BACHELOR THESIS IN PHYSICS

MODELLING IN-PLANE SPIN CURRENTS IN ATOMISTIC SPIN-DYNAMICS

by

CONSTANTIN DISSELKAMP

Submitted to the
FAKULTÄT FÜR MATHEMATIK, NATURWISSENSCHAFTEN UND INFORMATIK
of the Rheinisch-Westfälische Technische Hochschule Aachen

in
July 2017

written at the
Institute for Advanced Simulation (IAS)
Forschungzentrum Jülich

supervised by
Prof. Dr. Stefan Blügel

Constantin Dißelkamp: *Bachelor Thesis in Physics,*
Modelling in-plane spin currents in atomistic spin-dynamics,

SUPERVISORS:
Stefan Blügel
Gideon Müller

LOCATION:
Forschungzentrum Jülich

TIME FRAME:
Apr. 2017 to July 2017

CONTENTS

LIST OF FIGURES

LIST OF TABLES

INTRODUCTION

Magnets were already discovered in ancient times when humans observed the unusual behavior of lodestones. One of the first applications of magnetic materials were compasses and until today humans developed countless other applications. Especially the usage of magnets for data storage in modern technology is of particular importance since it has paved the way for the digital era we live in today. Despite the fact that magnets have been known to humans for thousands of years and that they are a keystone of our digital society, a full understanding of the microscopic processes that govern certain aspects of magnetism is still lacking.

Just recently in 2016 a Nobel prize was awarded for the work on topological phases of matter and phase transitions to David J. Thouless, F. Duncan M. Haldane and J. Michael Kosterlitz. The topological phase transition is driven by topological defects in the form of vortices and anti-vortices which separate under certain conditions similar to particles and anti-particles. Today topological vortices can be found in various research fields in all domains of physics. For instance, in condensed matter physics topological vortices are of relevance for spinfluid and suprafluid research and in the description of magnetic fields.

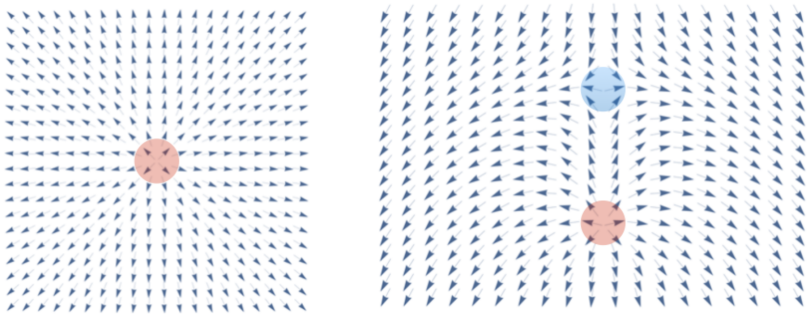

FIGURE I.1 – Vortices illustration

The picture shows a single and a vortex anti-votex pair in the XY-Heisenberg-model. This picture is taken from the information paper of the 2016 Nobel prize in physics [1].

In magnetic materials with Dzyaloshinskii-Moriya interaction (DMI) [2] those topological quasiparticles which form metastable states are called magnetic skyrmions. Magnetic skyrmions have been predicted theoretically

[3, 4, 5, 6, 7, 8, 9, 10] and observed experimentally [11] by various research groups.

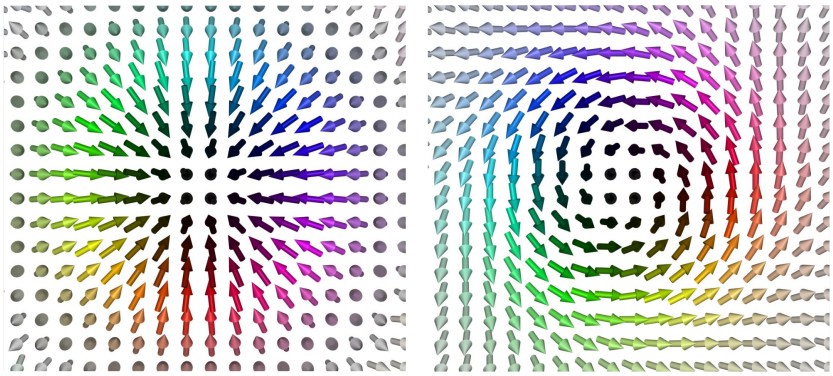

FIGURE I.2 – Visualisation of 2D Néel and Bloch type skyrmions

To the left a Néel type skyrmion, and to the right a Bloch type skyrmion. In the Néel type skyrmion the spins orient within the radial plane, while for the Bloch type skyrmion they orient perpendicular to the radial plane. Green denotes orientation in $+x$-direction (right for the reader), red in $+y$-direction (upwards), purple in $-x$-direction (left), blue in $-y$-direction (downwards) and the colour brightness denotes the orientation on the z-axis (bright $+z$- / dark $-z$-direction). The pictures were taken with *Spirit* [12].

Owing to their non trivial topology, magnetic skyrmions have been shown to possess novel and interesting transport properties and extraordinary stability [3, 4, 7, 9]. These fundamental discoveries in this new area have driven forward the proposal of new kinds of data storage devices.

In the last decades humans made impressive progress in developing ever faster and smaller computers. A primary ingredient for this progress is the development of new data storage devices, this makes skyrmions a very attractive field of research.

Memory in modern computers has to be fast in reading and writing data, have long lifetimes and, especially for the usage in mobile devices like mobile phones, tablets and laptops, energy efficiency and compact design are necessary. Conventional types of data storage are hard disk drives (HDDs) and flash storage. Flash storage is used in solid-state drives (SSDs), small portable data storage like USB flash drives and mobile devices. HDDs store data on magnetic material in which fixed energy minima, in the form of magnetic domains, which point in one of two directions, are being induced. They have the advantage of long lifetimes on the one hand, but due to their moving parts they are limited in speed and energy efficiency and are more vulnerable to concussions, what makes them, besides their size, impractical for mobile devices. SSDs use electronic circuits instead of

magnetised mediums as memory to store data and do not rely on moving components. SSDs have a shorter lifetime but faster read and write speeds prevail this in most cases. Magnetic storage is, due its reliability and price, prevailing in the ever growing marked of cloud centres. To eliminate the disadvantages and increase the storage density of magnetic storage would be a substantial progress.

With the topological comprehension of the effects inside magnetic material new ideas for realising memory devices came up. A very popular concept is domain wall racetrack memory [13, 14], a nanoscopic wire on which magnetic domains are moved by spin-polarised currents. The main problem of domain wall racetrack memory are impurities in the nano wire or spin chain. Impurities hinder the domain wall to travel and to overcome them high current densities have to be applied, which in turn leads to Joule heating of the nanowire and reveals limits of this approach.

This leads to the idea of skyrmion based memory (see also Figure I.3), which currently receives a lot of attention and is an important topic for many research groups [15, 16]. A significant advantage of skyrmion racetracks in comparison with domain wall racetracks, could be that they are able to overcome impurities more easily. For skyrmion based memory one needs to understand the properties of skyrmions with respect to external stimuli and perturbations and how to control their movement.

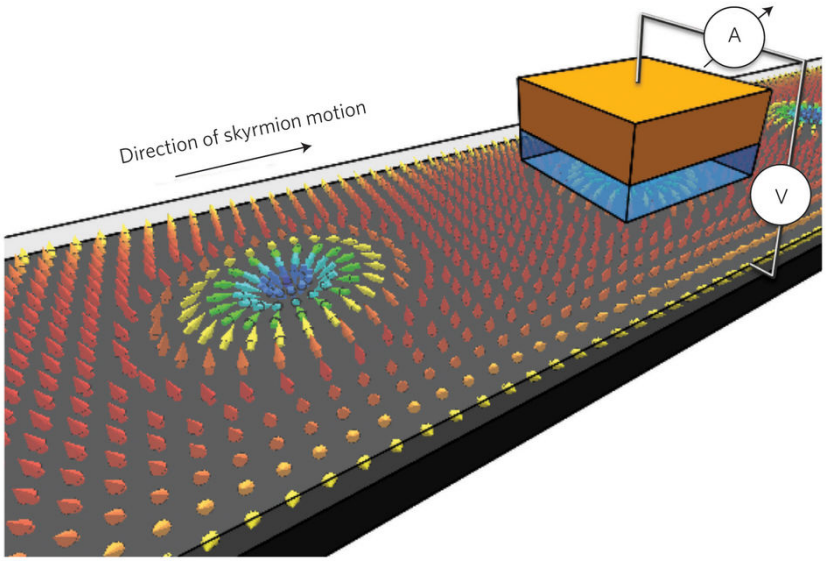

FIGURE I.3 – Schematic of a skyrmion based racetrack memory
The picture shows the racetrack and deployed skyrmions and also a tunnel junction read-out device (blue and orange boxes) in this picture. The picture taken from [17].

skyrmions in thin layers can be moved by applying a current perpendicular to the layer or in-plane. To solve the equations describing this movement analytically many approximations have to be made, hence it seems natural to use numerical methods, as they can capture a larger class of phenomena and lead to more precise solutions.

This thesis discusses spin-polarised currents, electrical currents, whose electrons have a common direction of motion and different spin-polarisation directions dependent on the magnetisation of the material, and investigates the movement of magnetic skyrmions generated by such currents. To accomplish this, a method to describe the interaction of spin-polarised currents with the magnetic system will be added to the existing spin simulation framework *Spirit* [12], for more details on the code see ref. [18]. We will refer to this method as the "gradient method", it will be implemented into the semi-implicit scheme B (SIB) method [19], a semi-implicit integration of the stochastic Landau-Lifschitz-Gilbert equation. The gradient method can also be used to model spin currents in any arbitrary direction in bulk material, which is interesting for fundamental research. In this Thesis we will confine to describing in-plane spin currents.

In Chapter 1 the basic atomistic model to effectively describe chiral magnets and the Landau-Lifschitz-Gilbert (LLG) equation which is used to describe spin dynamics will be introduced. These equations provide the basis for the numerical experiments performed within this thesis.
In Chapter 2 the numerical method which is used to solve the LLG equation is extensively described and the validity of the implementation of the gradient method into this integration scheme is annotated. Thereafter the spatial gradient which is used to describe the spin-polarised current is discussed and a numerical approximation, the difference quotient, is introduced. Based on the difference quotient, the transition to a model of spin transfer torque (STT)-induced spin current perpendicular to a monolayer is shown.
In Chapter 3 numerical results for a domain wall on a head to head spin chain and skyrmions on nanotracks with open boundary conditions are presented. The tests for the domain wall are primarily used to verify the validity of the implementation and are reproduced from the work of Schieback *et al.* [20]. Afterwards skyrmion motion is simulated on lattices with closed boundary conditions and on nanotracks. The velocity of the skyrmion is compared for different parameters of the LLG equation and further a comparison of in-plane current and perpendicular current is made.
In the Conclusion a short summary of this thesis is presented and prospects for the application of the gradient method are made.

THE MODEL 1

1.1 HEISENBERG MODEL

The quantum mechanical model to describe magnetic phases and magnetization processes in realistic systems is highly complex, which makes the description infeasible on a rigorous quantum-mechanical footing. Therefore we will be using the atomistic Heisenberg model, which can be considered as a semi-classical limit of a quantum-mechanical model. It considers the magnetic moments as classical vectors, localised on a lattice.

We now use the classical Heisenberg model to describe the properties of magnets that lead to stable skyrmion states. It reads, similar to the one shown in [20]:

$$\begin{aligned}\mathcal{H} = &-J\sum_{\langle ij\rangle}\mathbf{S}_i\cdot\mathbf{S}_j \; -K\sum_i(\hat{\mathbf{K}}\cdot\mathbf{S}_i)^2 \\ &-\mu_s\mathbf{B}\cdot\sum_i\mathbf{S}_i-\sum_{\langle ij\rangle}\mathbf{D}_{ij}\cdot(\mathbf{S}_i\times\mathbf{S}_j)\end{aligned} \tag{1.1}$$

where $\langle ij\rangle$ denotes summation over nearest neighbours. The spins $\mathbf{S}_i = \mu_i/\mu_s$ with $\mu_s = |\mu_i|$ the magnetic moment of a spin are located on a lattice. The first term is the isotropic exchange interaction between neighbouring spins with the ferromagnetic exchange coupling constant $J > 0$. In the case of ferromagnetic exchange interaction the spins $\mathbf{S}_i$ prefer to align parallel. The second term is the uniaxial anisotropic term with the unit vector $\hat{\mathbf{K}}$ pointing in the direction of the anisotropy easy axis and K denoting the magnitude. The third term includes coupling to a magnetic field $\mathbf{B}$. The last term is Dzyaloshinskii-Moriya interaction, it has an relativistic origin (spin-orbit coupling) and favours a spin canting, of otherwise (anti)parallel aligned magnetic moments.

1.2 LANDAU–LIFSHITZ–GILBERT EQUATION

We will have to describe the time evolution of the spin model introduced in 1.1. A classical equation of motion to describe the spin dynamics is the LLG-equation [21, 22, 23]. It can be extended to describe the effect of spin-polarised currents [24, 25, 26, 27]:

$$\begin{aligned}\frac{\partial \mathbf{S}_i}{\partial t} = &-\frac{\gamma}{\mu_s}\mathbf{S}_i \times \mathbf{H}_i - \alpha \mathbf{S}_i \times \frac{\partial \mathbf{S}_i}{\partial t} \\ &- u(\hat{\mathbf{j}}_e \cdot \nabla)\mathbf{S}_i + \beta u \mathbf{S}_i \times (\hat{\mathbf{j}}_e \cdot \nabla)\mathbf{S}_i \,.\end{aligned} \tag{1.2}$$

This implicit form can be easily translated to an explicit form as shown in [20]:

$$\begin{aligned}\frac{\partial \mathbf{S}_i}{\partial t} = &-\frac{\gamma}{(1+\alpha^2)\mu_s}\mathbf{S}_i \times \mathbf{H}_i - \frac{\gamma\alpha}{(1+\alpha^2)\mu_s}\mathbf{S}_i \times (\mathbf{S}_i \times \mathbf{H}_i) \\ &- \frac{\alpha-\beta}{(1+\alpha^2)} u \mathbf{S}_i \times (\hat{\mathbf{j}}_e \cdot \nabla)\mathbf{S}_i + \frac{1+\beta\alpha}{(1+\alpha^2)} u \mathbf{S}_i \times (\mathbf{S}_i \times (\hat{\mathbf{j}}_e \cdot \nabla)\mathbf{S}_i)\end{aligned} \tag{1.3}$$

with the effective fields $\mathbf{H}_i = -\partial\mathcal{H}/\partial\mathbf{S_i}$, the Gilbert damping constant α, the gyromagnetic ratio $\gamma = g\mu_B/\hbar$ and constant non-adiabaticity parameter β. u is given by $u = j_e P g \mu_B/(2eM_s)$ with the absolute value of the current density j_e, polarisation P, saturation magnetisation M_s, Landé g-factor g, magnitude of electron charge e and Bohr magneton μ_B. $\mathbf{S}_i$ is a 3D magnetic moment of unit length and denotes the spin on lattice site i. The current density vector of unit length $\hat{\mathbf{j}}_e = \mathbf{j}_e/j_e$ points in the direction of the polarised current.

The first Term of Equation 1.3 describes the precession of the magnetic moment $\mathbf{S}_i$ within the effective field $\mathbf{H}_i$. The second Term describes the relaxation of the magnetic moment. Term three and four include a spin-polarised current. The expression $(\hat{\mathbf{j}}_e \cdot \nabla)$ denotes a spatial gradient of the magnetisation in real space. The spatial gradient expresses the rate of change of the spins at the given position, it will be discussed more precise later.

A full quantum mechanical definition of spin-polarised currents is given by Z. An *et al.* [28]. As expected, the spin current operator, which is defined as $J_S = \frac{i}{2}(\hat{\alpha}_\mu \hat{\Sigma}_\nu)$, consists of a velocity operator $\hat{\alpha}$ and a spin operator $\hat{\Sigma}$.

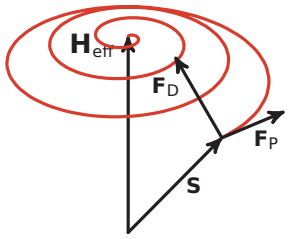

FIGURE 1.1 – Damped spin precession

The first and the second term of Equation 1.3 are visualised as the vectors $\mathbf{F}_P$ and $\mathbf{F}_D$. The red line denotes the classical trajectory the spin takes. The precession term $\mathbf{F}_P$ leads to a precession around the effective Field, the damping term $\mathbf{F}_D$ pulls the spin towards the effective Field. Spin length is conserved since the forces are perpendicular to the spin. Picture taken from [29].

The fourth term in Equation 1.2 is a correction term for the spin-polarised current. It got introduced since qualitative findings by micromagnetic computations [24] uncovered discrepancies with experimental results. The modified LLG equation is shown and discussed by Thiaville *et al.* [26].

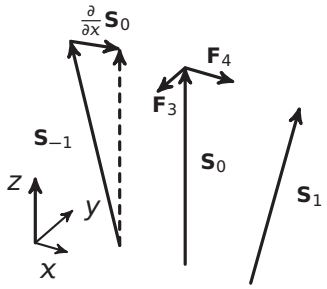

FIGURE 1.2 – Forces added by spin-polarised current

This figure shows a schematic visualisation for the third and fourth term in Equation 1.3 for the spin current density $\hat{\mathbf{j}}_e = \mathbf{e}_x$, named $\mathbf{F}_3$ and $\mathbf{F}_4$. Spin length is conserved since the forces are perpendicular to the spin.

To add thermal fluctuations to the LLG-equation, we add a thermal noise term $\zeta_i(t)$ to the effective field [20]:

$$\mathbf{H}_i = -\frac{\partial \mathcal{H}}{\partial \mathbf{S}_i} + \zeta_i(t)\,. \tag{1.4}$$

The thermal noise term $\zeta_i(t)$ has the properties of white noise. It is normally distributed, has zero mean and variance

$$\langle \zeta_i^2(t) \rangle = 2\frac{\alpha \mu_s}{\gamma} k_B T \tag{1.5}$$

with k_B the Boltzmann constant and temperature T.
Since we solve the equation by calculating discrete time steps δt, the variance has to be normalised with respect to the time step:

$$\langle \zeta_i^2(t) \rangle = \xi^2 \delta t \quad \text{with} \quad \xi = \sqrt{\frac{2\frac{\alpha\mu_s}{\gamma} k_B T}{\delta t}} \tag{1.6}$$

In this Chapter we obtained all equations we need to describe all kinds of spin dynamics. We also included modulation of spin currents in arbitary directions. The next step is to solve the equations. We will approach this with numerical methods.

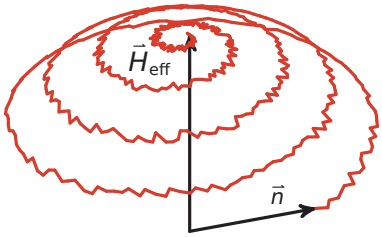

FIGURE 1.3 – Stochastic and damped spin precession

Schematic representation of the spin precession under influence of the stochastic noise term. Since the stochastic noise ζ is applied perpendicular to the spin, spin length is conserved. Picture taken from [29].

To compare Equation 1.3 to the LLG equation used by Schieback *et al.* [20] we consider a current in x-direction with $\hat{\mathbf{j}}_e = \mathbf{e}_x$, we then obtain $(\hat{\mathbf{j}}_e \cdot \nabla) = \frac{\partial}{\partial x}$ for the spatial gradient. We note that in that case Equation 1.3 is equivalent to the one used by Schieback *et al.*.

In Equation 1.3 we see an ansatz capable of modelling the spin transfer torque in bulk materials. The current implementation in *Spirit*, based on the LLG equation derivated in [30], can only simulate the effect of a spin current perpendicular to a single-free-layer framed in pinned-layers (see Figure 2.1). In this case the magnetic moment of the spin current is described by a constant vector $\mathbf{S}_p$ of unit length which points in the direction of the pinned-layer and the third and forth term of Equation 1.3 are in that case proportional to $-\mathbf{S} \times \mathbf{S}_p$ and $\mathbf{S} \times (\mathbf{S} \times \mathbf{S}_p)$, with prefactors proportional to the spin current. This approximation solely works for the pinned-layer - single-free-layer - pinned-layer case. The transition between both methods will be discussed in Section 2.3.

NUMERICAL METHODS 2

Some partial differential equations, like the LLG equation (1.3) we introduced in the previous Chapter can not be rigorously solved by analytical approaches. Therefore one needs to use numerical methods to obtain accurate results.

2.1 SOLVING THE LLG EQUATION WITH THE SIB METHOD

We will now use the SIB method which was introduced by Mentink *et al.* [19] to solve the LLG equation (1.3). The SIB method consists of two iteration steps, the SIBt (semi-implicit B temporal) and the SIBf (semi-implicit B final). Both steps use the implicit midpoint (IMP) structure to preserve the spin length while SIBt calculates a predictor and SIBf uses the predictor to calculate the new orientation of the spin $\mathbf{S}$ after the time step δt. We annotate the spin at time t_0 as $\mathbf{S}_n$ and at time $t_0 + \delta t$ as $\mathbf{S}_{n+1}$, thus in this section the index n of $\mathbf{S}$ denotes a step in time and not the position of the spin.

Before applying the SIB method we rearrange Equation 1.3 to:

$$\frac{\partial \mathbf{S}_i}{\partial t} = \mathbf{S}_i \times \mathbf{A}(\mathbf{S}_i)\,, \tag{2.1}$$

where

$$\begin{aligned}\mathbf{A}(\mathbf{S}_i) = &-\frac{\gamma}{(1+\alpha^2)\mu_s}\mathbf{H}_i + \frac{\gamma}{(1+\alpha^2)\mu_s}\alpha(\mathbf{S}_i \times \mathbf{H}_i) \\ &-\frac{\alpha-\beta}{(1+\alpha^2)}u(\hat{\mathbf{j}}_e \cdot \nabla)\mathbf{S}_i + \frac{1+\beta\alpha}{(1+\alpha^2)}u(\mathbf{S}_i \times (\hat{\mathbf{j}}_e \cdot \nabla)\mathbf{S}_i)\,.\end{aligned} \tag{2.2}$$

This form can now be used in the SIB-method.

The implicit midpoint method, which the SIB method bases on, solves differential equations of the form $y'(t) = f(t, y(t))$, $y(t_0) = y_0$ and an

iteration step is defined as

$$y_{n+1} = y_n + h \cdot f\left(t_n + \frac{h}{2}, \frac{y_n + y_{n+1}}{2}\right). \tag{2.3}$$

For the LLG equation 2.1 and the time step δt this leads us to

$$\mathbf{S}_{n+1} = \mathbf{S}_n + \delta t \frac{\mathbf{S}_n + \mathbf{S}_{n+1}}{2} \times \mathbf{A}\left(\frac{\mathbf{S}_n + \mathbf{S}_{n+1}}{2}\right). \tag{2.4}$$

The semi-implicit scheme B (SIB) uses a predictor $\tilde{\mathbf{S}}$ to reduce the implicitness of the equation above by replacing $\mathbf{S}_{n+1}$ in the argument of $\mathbf{A}$. To preserve spin length the predictor is obtained with the spin length conserving IMP structure.

We start with the SIBt to obtain a predictor:

$$\tilde{\mathbf{S}} = \mathbf{S}_n + \delta t \frac{\mathbf{S}_n + \tilde{\mathbf{S}}}{2} \times \mathbf{A}(\mathbf{S}_n). \tag{2.5}$$

First we have to calculate $\mathbf{A}(\mathbf{S}_n) = \mathbf{A}(\mathbf{H}, \mathbf{S}_n) + \mathbf{A}_{rnd}(\zeta, \mathbf{S}_n)$ where we have separated the thermal (stochastic) term from $\mathbf{H}$. $\mathbf{A}_{rnd}$ simulates white noise which models the thermal fluctuations.

When multiplying $\delta t/2$ to the field in Equation 2.5 we have to consider Equation 1.6 for the thermal term:

$$\mathbf{A}_{\delta t} = \frac{1}{2}(\delta t \cdot \mathbf{A} + \sqrt{\delta t} \cdot \mathbf{A}_{rnd}) \tag{2.6}$$

With $\mathbf{A}_{\delta t}$ Equation 2.5 can be rewritten as:

$$\mathbf{M} \cdot \tilde{\mathbf{S}} = \mathbf{M}^T \cdot \mathbf{S}_n \tag{2.7}$$

$$\text{with matrix} \quad \mathbf{M} = \mathbf{I} + \text{skew}(\mathbf{A}_{\delta t}) = \begin{pmatrix} 1 & -A_z^{\delta t} & A_y^{\delta t} \\ A_z^{\delta t} & 1 & -A_x^{\delta t} \\ -A_y^{\delta t} & A_x^{\delta t} & 1 \end{pmatrix}.$$

The right side of Equation 2.7 can be easily calculated from the given parameters:

$$\mathbf{M}^T \cdot \mathbf{S}_n = \mathbf{S}_n + \mathbf{S}_n \times \mathbf{A}_{\delta t} =: \boldsymbol{\alpha}.$$

To solve Equation 2.7 we use Cramer's rule. The components $\tilde{S}^\alpha$ with $\alpha = x, y, z$ of $\tilde{\mathbf{S}}$ are calculated with

$$\tilde{S}^\alpha = \frac{\det(\mathbf{M}^\alpha)}{\det(\mathbf{M})}$$

where $\mathbf{M}^{\alpha}$ is the same matrix as $\mathbf{M}$ but column α is replaced with the vector $\mathbf{a}$, for example

$$\mathbf{M}^{x} = \begin{pmatrix} a_x & -A_z & A_y \\ a_y & 1 & -A_x \\ a_z & A_x & 1 \end{pmatrix}.$$

We now use the predictor $\tilde{\mathbf{S}}$ in the SIBf step to calculate $\mathbf{S}_{n+1}$:

$$\mathbf{S}_{n+1} = \mathbf{S}_n + \delta t \frac{\mathbf{S}_n + \mathbf{S}_{n+1}}{2} \times \mathbf{A}\left(\frac{\mathbf{S}_n + \tilde{\mathbf{S}}}{2}\right). \tag{2.8}$$

The SIBf step is mostly analogue to the SIBt step, see analogy between Equation 2.5 and 2.8, but now we calculate the fields from $(\mathbf{S}_n + \tilde{\mathbf{S}})/2$. Therefore we have to use $\mathbf{A}(\mathbf{H}, (\mathbf{S}_n + \tilde{\mathbf{S}})/2)$ and $\mathbf{A}_{rnd}(\zeta, (\mathbf{S}_n + \tilde{\mathbf{S}})/2)$.

Mentink *et al.* [19] showed this method for the LLG equation without spin transfer torque. Adding the spin transfer torque terms to $\mathbf{A}$ can be done without further ado and no special normalization is needed, since they do not include statistical processes. Furthermore this is verified by the reproduction of numerical results of Schieback *et al.* [20] in Chapter 3.

2.2 SPATIAL GRADIENT

For the implementation of the gradient method we have to determine a numerical method to calculate the spatial gradient. The spatial gradient occurs in equation 2.2 in the context: $(\hat{\mathbf{j}}_e \cdot \nabla)\mathbf{S}_i$. The finite difference quotient will be used to obtain a good approximation.

The expression $(\hat{\mathbf{j}}_e \cdot \nabla)\mathbf{S}_i$ can also be written as:

$$(\hat{\mathbf{j}}_e \cdot \nabla)\mathbf{S}_i = j_e^x \cdot \frac{\partial \mathbf{S_i}}{\partial x} + j_e^y \cdot \frac{\partial \mathbf{S_i}}{\partial y} + j_e^z \cdot \frac{\partial \mathbf{S_i}}{\partial z} \tag{2.9}$$

where j_e^x, j_e^y, j_e^z denote the cartesian components of the spin current $\hat{\mathbf{j}}_e$ of unit length and $\partial \mathbf{S_i}/\partial\alpha$ with $\alpha = x, y, z$ are the partial derivatives of the spin in all positive cartesian directions.

What we see above is the vector gradient $\mathrm{grad}(\mathbf{S}_i)$ calculated in the direction of $\hat{\mathbf{j}}_e$. The vector gradient maps vector fields $\vec{F}\colon \mathbb{V}^n \to \mathbb{V}^m$ from the euclidean vector space $\mathbb{V}^n$ to a vector space $\mathbb{V}^m$ and is defined as:

$$\mathrm{grad}(\vec{F}) = (\vec{\nabla} \otimes \vec{F})^T = (\vec{\nabla}\vec{F})^T \in \mathbb{V}^n \otimes \mathbb{V}^n. \tag{2.10}$$

With the vector gradient we can calculate the directional derivative of a vector field in the direction of a vector $\vec{h} \in \mathbb{V}^n$:

$$\mathrm{grad}(\vec{F}) \cdot \vec{h} = (\vec{\nabla} \otimes \vec{F})^{\mathsf{T}} \cdot \vec{h} = \vec{h} \cdot (\vec{\nabla} \otimes \vec{F}) = (\vec{h} \cdot \vec{\nabla})\vec{F}\,. \tag{2.11}$$

We will now use the difference quotient to get a good approximation for the derivatives in Equation 2.9. The following calculations are lattice dependent, but as an example we will now consider a cubic lattice. The difference quotient of the magnetic moment between neighbouring spins on a cubic lattice in x-direction is calculated as follows:

$$\frac{\partial \mathbf{S}_i}{\partial x} = \frac{\mathbf{S}_{i+} - \mathbf{S}_i}{t_x} \tag{2.12}$$

where $\mathbf{S}_{i+}$ is the neighbour in x-direction of $\mathbf{S}_i$ and t_x the absolute value of the translation vector, respectively the lattice constant, in x-direction. To obtain a more precise value we can calculate the difference quotient in forward and backward direction and take the mean:

$$\frac{\partial \mathbf{S}_i}{\partial x} = \frac{1}{2}\left(\frac{\mathbf{S}_{i+} - \mathbf{S}_i}{t_x} - \frac{\mathbf{S}_{i-} - \mathbf{S}_i}{t_x}\right) = \frac{\mathbf{S}_{i+} - \mathbf{S}_{i-}}{2t_x} \tag{2.13}$$

where $\mathbf{S}_{i-}$ is the neighbour in $-x$-direction of $\mathbf{S}_i$.
If we repeat this for the derivatives in x and z-direction we can calculate the spatial gradient for the cubic lattice and a spin-polarised current in any direction with Equation 2.9.

One could consider to only calculate the difference quotient in backward direction relative to the spin current direction $\hat{\mathbf{j}}_e$ and multiply the result by -1. Intuitively this seems, considering the atomistic model, to be the most physical approach, since the last spin which a electron of the spin current interacts with before interacting with the spin S_i, is the one in opposite direction of the spin current. However to calculate this can become very complex considering spin currents in arbitrary directions and more complex lattices. For all cases relevant to this thesis the approach in Equation 2.13 is convenient.

For arbitrary lattices the translation vectors need not be parallel to the euclidean x-, y- or z-axis. Therefore we have to project the difference quotients on the basis vectors of the coordinate system. Exemplary we consider a lattice with six neighbours, respectively two neighbours symmetrical in the exact opposite direction, similar to a cubic lattice but with non-perpendicular translation vectors. We have to project the derivatives in arbitrary directions on each direction in cartesian space, exemplary we

obtain the x-direction from:

$$2\frac{\partial \mathbf{S}_i}{\partial x} = (\vec{e}_x \cdot \vec{t}_a)\frac{\partial \mathbf{S}_i}{\partial a} + (\vec{e}_x \cdot \vec{t}_b)\frac{\partial \mathbf{S}_i}{\partial b} + (\vec{e}_x \cdot \vec{t}_c)\frac{\partial \mathbf{S}_i}{\partial c} \\ (\vec{e}_x \cdot (-\vec{t}_a))\frac{\partial \mathbf{S}_i}{\partial (-a)} + (\vec{e}_x \cdot (-\vec{t}_b))\frac{\partial \mathbf{S}_i}{\partial (-b)} + (\vec{e}_x \cdot -(\vec{t}_c))\frac{\partial \mathbf{S}_i}{\partial (-c)}, \tag{2.14}$$

$\vec{t}_m$ $(m = a, b, c)$ are the translation vectors pointing to the (forward) neighbours and $\partial \mathbf{S}_i / \partial m$ $(m = a, b, c)$ are the difference quotients in the direction of the translation vectors, whereby $\partial \mathbf{S}_i / \partial (-m)$ are the difference quotients in negative translation vector direction. In this case we obtain a difference quotient in the form of Equation 2.13 for each two difference quotients in $\vec{t}_a$ and $-\vec{t}_a$ direction.

In general we can use:

$$\frac{\partial \mathbf{S}_i}{\partial x} = \frac{1}{2}\sum_{j=1}^{N}(\vec{e}_x \cdot \vec{t}_{a_j})\frac{\partial \mathbf{S}_i}{\partial a_j} \tag{2.15}$$

for lattices with N nearest neighbours and every neighbour, with translation vector $\vec{t}_{a_j}$, has an $180°$ opposing neighbour. However for open boundary conditions we have to consider the spins on the edges which have no opposing neighbour in that case we only obtain one difference quotient on a certain line (in forward and backward direction) and have to strike the factor $1/2$ off.

In the same manner we obtain the difference quotients in y and z-direction. We are now again able to calculate the spatial gradient in Equation 2.9.

This is also possible in lower dimensions. In N-dimensions one needs a minimum of N linear independent neighbours to calculate Equation 2.9 with $\hat{\mathbf{j}}_e$ pointing in an arbitrary direction. For the purpose of this thesis we only need to calculate the spatial gradient in high symmetrical lattices, a spin chain and a two dimensional cubic lattice.

2.3 TRANSITION TO PINNED-LAYER MODEL

In 2016 Daniel Schürhoff [18] already implemented a method into the SIB method to model spin-polarised currents. However the method is only capable of modelling spin currents for specific use cases, where the gradient method should be able to model spin currents in a larger set of cases.

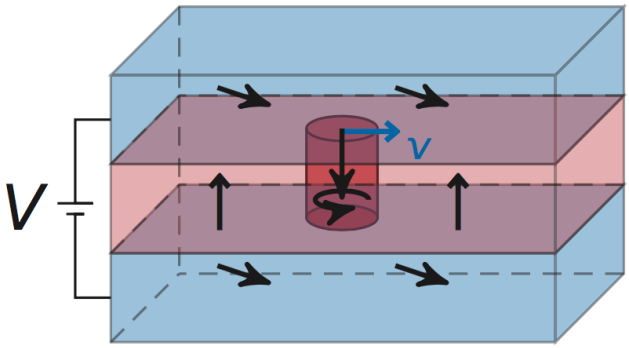

FIGURE 2.1 – Layer model for current induced skyrmion motion

The graphic shows a three layer system, two pinned-layers (blue), where the spins are pinned in a certain direction and a free-layer (red), a one atom thick layer whose spins are not pinned. Between the two pinned-layers a voltage gets applied, what leads to a current perpendicular to the free-layer. The cylinder represents a skyrmion which gets moved by the spin current. Picture taken from [18], slightly modified, to show the orientation of the spins in the pinned layer.

With the knowledge about the spatial gradient and the difference quotient as a good numerical approximation we can now show the transition of the gradient method to the previous implementation of the spin current.

The previous implementation was based on the work of Chureemart *et al.* and S. Zhang *et al.* [25, 27, 30, 31, 32]:

$$\frac{\partial \mathbf{S}_i}{\partial t} = -\gamma \mathbf{S}_i \times \mathbf{H}_i + \alpha \mathbf{S} \times \frac{\partial \mathbf{S}_i}{\partial t} + \gamma a_j \mathbf{S} \times (\mathbf{S}_i \times \mathbf{S}_p)\,. \tag{2.16}$$

The implicit form above can be translated to an explicit form:

$$\begin{aligned} \frac{\partial \mathbf{S}_i}{\partial t} = &- \frac{\gamma}{(1+\alpha^2)\mu_s} \mathbf{S}_i \times \mathbf{H}_i - \frac{\gamma\alpha}{(1+\alpha^2)\mu_s} \mathbf{S}_i \times (\mathbf{S}_i \times \mathbf{H}_i) \\ &- \frac{\gamma\alpha a_j}{(1+\alpha^2)} \mathbf{S}_i \times \mathbf{S}_p + \frac{\gamma a_j}{(1+\alpha^2)} \mathbf{S}_i \times (\mathbf{S}_i \times \mathbf{S}_p)\,, \end{aligned} \tag{2.17}$$

with $\mathbf{S}_p$ the spins of the pinned-layer and parameter a_j, which is proportional to spin current density, but not further determined. The non-adiabatic term with factor β was not implemented in this version.

We will first take a look at the third term in Equation 1.2. It can be motivated similar to the motivation by S. Zhang *et al.* [31]. To obtain the term we look at the derivative of the spin current density $\mathbf{j}_x/M_s = g\mu_B P j_e \mathbf{S}/(2eM_s)$. For simplicity we first consider a spin current pointing in

x-direction, this leads to:

$$\tau \equiv \frac{\partial \mathbf{j}_x(x,t)/M_s}{\partial x} = u\frac{\partial \mathbf{S}}{\partial x} \tag{2.18}$$

with $u = j_e P g \mu_B/(2eM_s)$. As described in ref. [31] we may make use of the fact that the magnitude of the magnetization is a constant at temperature well below the Curie temperature, we can rewrite the spin torque as:

$$\tau = -u\mathbf{S} \times (\mathbf{S} \times \frac{\partial \mathbf{S}}{\partial x}) . \tag{2.19}$$

For a spin current in arbitrary direction we replace $\partial\mathbf{S}/\partial x$ and obtain:

$$\tau = -u\mathbf{S} \times (\mathbf{S} \times (\hat{\mathbf{j}}_e \cdot \nabla)\mathbf{S}) , \tag{2.20}$$

this form is conform with the third term in Equation 2.16.

The transition from the gradient method to the pinned-layer/free-layer case can now be shown by using the difference quotient to calculate the gradient (see Section 2.2). In the following we consider a spin current $\hat{\mathbf{j}}_e = \mathbf{e}_x$ perpendicular to a free layer in the yz-plane. The backward neighbour in spin current direction of the spin in the free layer is $\mathbf{S}_p$. For the inner cross product in Equation 2.20 this leads to:

$$\mathbf{S}_i \times (\hat{\mathbf{j}}_e \cdot \nabla)\mathbf{S}_i = \mathbf{S}_i \times \frac{\partial \mathbf{S}_i}{\partial x} = \mathbf{S}_i \times \left(-\frac{\mathbf{S}_p - \mathbf{S}_i}{t_x}\right) = \frac{-1}{t_x}\mathbf{S}_i \times \mathbf{S}_p \tag{2.21}$$

The neighbour opposite to the spin current direction is the last spin which the spin of the current interacts with before interacting with $\mathbf{S}_i$. Therefore we have to use the difference quotient in opposite direction of the current and multiply it by -1.

When we now plug the result in Equation 2.20, we obtain:

$$\tau_b = +\frac{u}{t_x}\mathbf{S} \times (\mathbf{S} \times \mathbf{S}_p) , \tag{2.22}$$

comparing this with the third term in Equation 2.16, gives us a relation between the pre factors $\gamma a_j = u/t_x$ and shows the same structure and correct sign. t_x in this case represents the layer thickness, since it denotes the distance between the spins $\mathbf{S}_p$ of the pinned-layer and $\mathbf{S}$ of the free-layer.

NUMERICAL RESULTS 3

The method introduced in the previous chapter will now be tested and used for simulating domain wall and skyrmion movement caused by in-plane spin currents. First the results for domain wall motion obtained by Schieback *et al.* [20] will be reproduced and afterwards skyrmion motion will be analysed in general and on a nano-track.

3.1 DOMAIN WALL MOTION

To test the implementation of the gradient method we will reproduce the results from the work of Schieback *et al.* [20]. They studied the behaviour of a domain wall on a head to head spin chain.

FIGURE 3.1 – Domain wall on head to head spin chain

The figure shows the initial spin configuration of the domain wall corresponding to Equation 3.1. All spins are oriented in the xy-plane (parallel to the paper). Green denotes orientation in positive x-direction (right for the reader), red in positive y-direction (upwards) and purple in negative x-direction (left). Picture was taken with *Spirit*.

The chain is oriented along the x-axis and the first and the last spin are fixed in $+x$ and $-x$ direction, respectively. We adjusted three spins in the middle of the chain forming a domain wall and then used direct energy minimization to relax them. We obtain a spin chain as shown in Figure 3.1. Schieback *et al.* [20] used the following description for the spin orientations:

$$\mathbf{S}(x) = -\tanh\left(\frac{x}{W}\right)\mathbf{e}_x + \frac{\cos(\phi)}{\cosh(\frac{x}{W})}\mathbf{e}_y + \frac{\sin(\phi)}{\cosh(\frac{x}{W})}\mathbf{e}_z\,. \tag{3.1}$$

The final spin orientations after the relaxation with the direct energy minimization and the theoretical description in Equation 3.1 matched very well. Therefore we can use the domain wall as the starting configuration for the following tests.

The Hamiltonian for this system can be written as follows [20]:

$$\mathcal{H} = -J \sum_{\langle ij \rangle} \mathbf{S}_i \cdot \mathbf{S}_j - K_1 \sum_i (\hat{\mathbf{K}}_1 \cdot \mathbf{S}_i)^2 - K_2 \sum_i (\hat{\mathbf{K}}_2 \cdot \mathbf{S}_i)^2 \,, \tag{3.2}$$

the terms were already described in Section 1.1, in this case a second uniaxial anisotropy term is added. $\hat{\mathbf{K}}_1$ points in x-direction and $\hat{\mathbf{K}}_2$ in y-direction.

The domain wall in Figure 3.1 and the following simulations all use the parameters listed in Table 3.1.

Parameter	Value	Unit
J	1	meV
a	1	Å
K_1	0.01	meV
K_2	0.005	meV
μ_s	2	μ_B
T	0	K

TABLE 3.1 Domain wall parameters

For the following numerical experiments the damping was set to $\alpha = 0.02$, the non-adiabatic parameter to $\beta = 0$, the time step was chosen to be $\delta t = 20$fs (see Equation 2.4) and the chain size was chosen to be 513 or 1025 lattice sites, except for the long term velocity measurements where sizes up to 2562 lattice sites where needed.

To illustrate the effect of a spin current on the domain wall, the initial spin orientations and the orientations after 10ns are shown in Figure 3.2. We can already see, that the domain wall tilting out of the xy-plane by a small angle since the z-component increases. A decrease of the domain wall width is also visible.

We will now go in greater detail and investigate the behaviour of the domain wall in respect to the distance x_{max} it travels before it stops moving forward, the angle ϕ it tilts out of the xy-plane, its width W and the

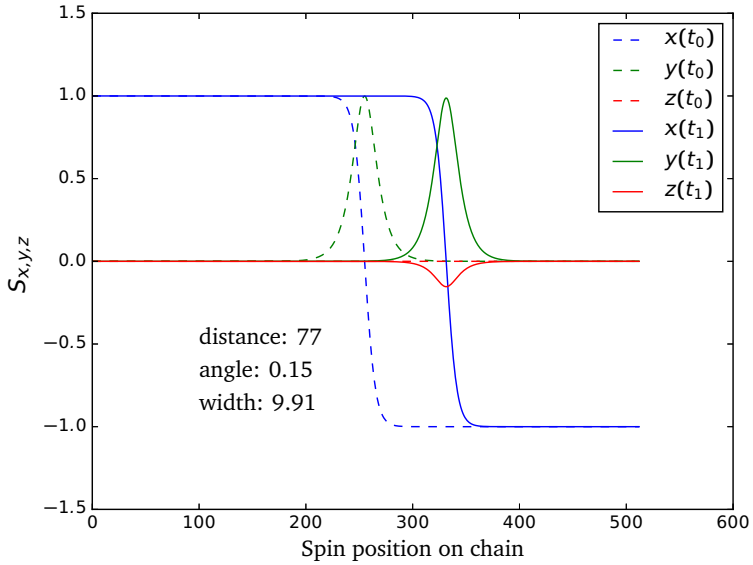

FIGURE 3.2 – Spin orientations - DW translation by spin current
In dashed lines the initial orientations of the spins is shown, which match the theoretical description by Equation 3.1. The other lines show the spin orientations after the domain wall was exposed to a spin current ($u\mu_s/(Ja\gamma) = 0.04$) for 500000 iterations, respectively 10ns. The initial domain wall width was $W \approx 10.02a$, distance 0 and angle $\phi = 0$.

average velocity $\langle v \rangle$ it reaches for different non-adiabatic parameters β. All properties are obtained in dependence of the magnitude of the applied spin current.

For currents below the walker breakdown [33], a phenomenon first observed for domain walls driven by external magnetic fields [33, 34, 35], but also observed for current driven domain walls [25, 26], and $\beta = 0$ the domain wall only moves a distance x_{max} and then stops, this is shown in Figure 3.3. The constraint of the travelled distance is to trace back to the domain wall tilting out of the xy-plane by a small angle ϕ like seen in Figure 3.4.

The applied current also decreases the width of the domain wall. To determine the width of the domain wall at a given time the derivation of the x-component in Equation 3.1 is taken. At $x = 0$ this yields to $d/dx(-\tanh(x/W))|_{x=0} = -1/W$. Now the derivation can be numerically computed from the data and we obtain the width W. The results for the domain wall widths are shown in Figure 3.5.

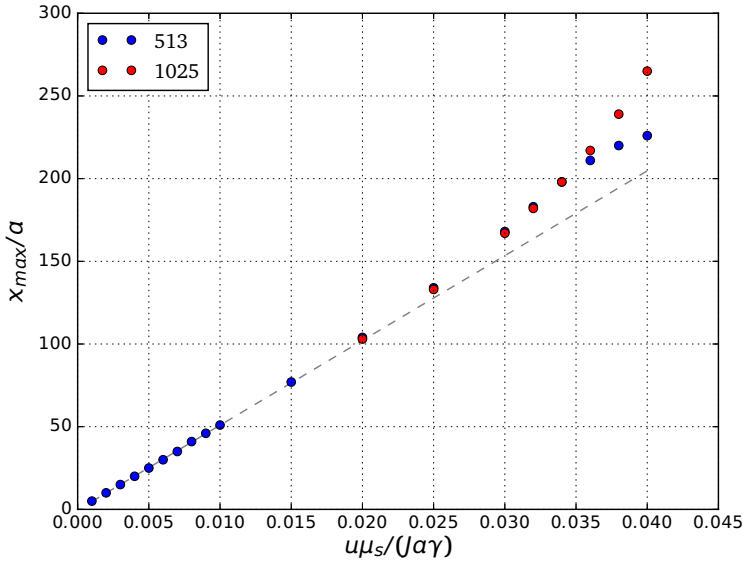

FIGURE 3.3 – Displacement of the domain wall

Maximum travelled distance x_{max} for different spin currents. The non-adiabatic parameter was set to $\beta = 0$ and damping to $\alpha = 0.02$. Blue dots denote measurements on the 513, red ones on the 1025 lattice sites chain. For higher currents the domain wall on the 513 sites chain was too close to the pinned end and got reflected at the end. This lead to a smaller maximum displacement as seen in the figure. The dashed line shows a linear fit for small u.

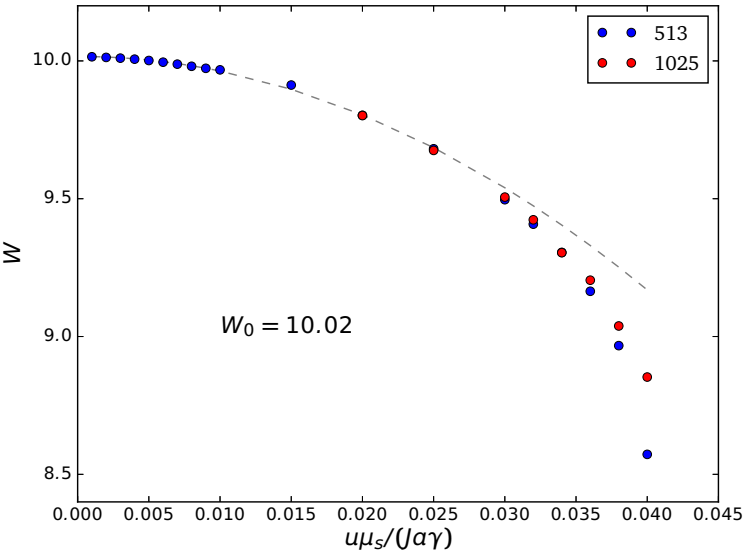

FIGURE 3.5 – Final width of the domain wall

The domain wall width W in units of lattice sites $a = 1$ after the wall stopped moving for different spin currents. The distortion can be described by $W/W_0 \approx 1 - C \cdot u_x^2$ for small currents, the line shows a fit to the data.

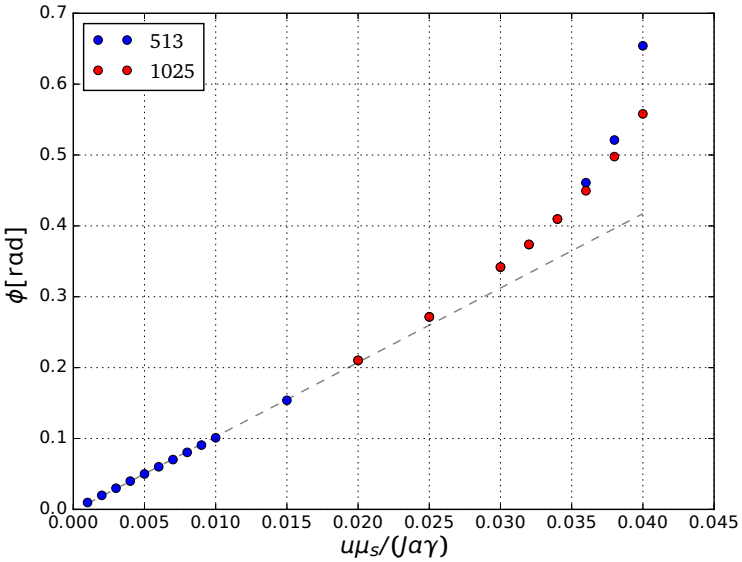

FIGURE 3.4 – Maximum out of plane angle of the domain wall

The maximum out of plane angle ϕ reached by the domain wall, when it stops moving, in dependence on the spin current. The non-adiabatic parameter was set to $\beta = 0$ and damping to $\alpha = 0.02$. The dashed line shows a linear fit for small u.

Schieback *et al.* used the analytical results, describing the behaviour of the domain wall, obtained by Li *et al.* [27] to fit the data. The same formulas were used to fit the data produced for this thesis and a good agreement, between the data and the analytical predictions for small currents u, was obtained. The deviations obtained for larger currents are expected, since the assumption made by the analytical calculations, that the domain wall shape remains in the standard transverse domain wall is only valid for small currents. The deviation for large currents occurs in Figure 3.3, Figure 3.4 and Figure 3.5.

Finally, the results for the domain wall velocity for different non-adiabatic parameters β, were reproduced. The results can be seen in figure 3.6. In agreement with the results of Schieback *et al.* we observed the Walker breakdown and a critical effective velocity u_c.

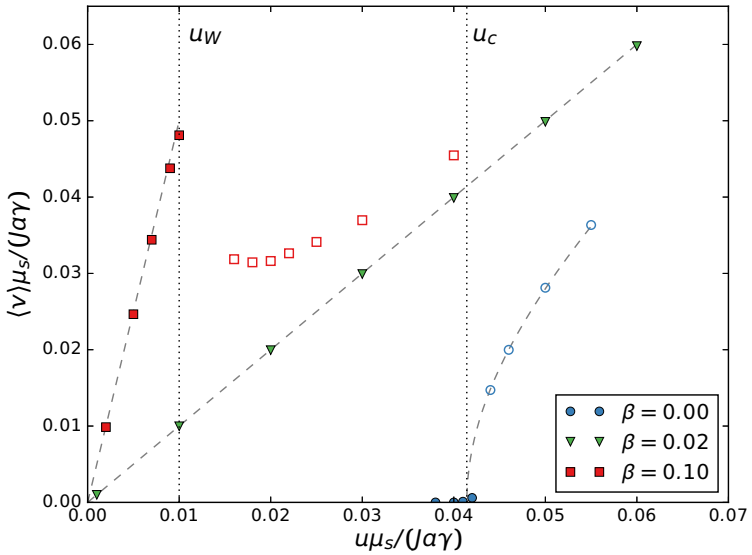

FIGURE 3.6 – Average velocity of the domain wall

The average velocity for different non-adiabatic parameters β. For $\beta = 0.10$ we observe the Walker breakdown at approximately $u_W \approx 0.01$. For $\beta = 0$ we can observe a critical current at $u_c \approx 0.0414$, from this point the relation $\langle v \rangle = \sqrt{u^2 - u_c^2}/(1+\alpha^2)$ mentioned by Thiaville *et al.* [24] takes effect. The mentioned relation is fitted to the data for $\beta = 0$. For $\beta = 0.1$ and currents under the walker breakdown and $\beta = 0.02$ the dashed lines show linear fits. Open symbols denote rotation around the x-axis.

The approximate prediction $\langle v \rangle = \sqrt{u^2 - u_c^2}/(1+\alpha^2)$ derived by Thiaville *et al.* [24] fits very well to our data in Figure 3.6 and we observe a critical current of $u_c \approx 0.0414$, Schieback *et al.* observed a value of $u_c \approx 0.0416$ which is very close. For $\beta = 0.1$ and currents larger than u_W and for $\beta = 0$ and currents larger than u_c, the wall starts rotating around the x-axis.
The slightly deviation, from the results by Schieback *et al.*, for the measured points at $u\mu_s/(J a \gamma) \approx 0.04$ for $\beta = 0$ and $u\mu_s/(J a \gamma) \approx 0.015$ for $\beta = 0.10$ are probably due to insufficient simulation time.

All results shown by Schieback *et al.* [20] could be well reproduced. The results strengthen the validity of the implementation of the gradient method into the SIB method as well as the underlying framework which is part of *Spirit*.

3.2 SKYRMION MOTION

We will now use the gradient method to model in-plane spin currents in two dimensional lattices and study the precipitated skyrmion motion. For this simulation Equation 1.1 is used, the values of the parameters are listed in Table 3.2. The damping was set to $\alpha = 0.02$ for all following simulations and the time step was chosen to be $\delta t = 2\text{fs}$.

Parameter	Value	Units
μ_s	2	μ_B
$\|B\|$	24	T
J	10	meV
K	0	meV
μ_s	2	μ_B
D	6	meV

TABLE 3.2 Parameters for skyrmion simulations

We start by simulating in-plane current in a quadratic 50×50 lattice with closed boundary conditions in x- and y-direction to obtain a first qualitative insight about the skyrmion motion (Figure 3.7).

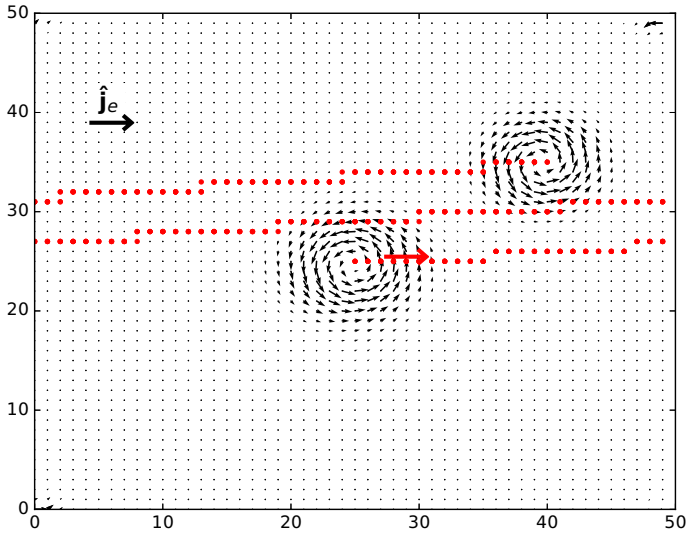

FIGURE 3.7 – Skyrmion motion with closed boundary conditions

The graph shows the initial skyrmion position with no applied current located in the middle and the position after a current was applied in x-direction for a total time of 0.98ns. The applied current is proportional to $u = 0.04$. The non-adiabatic constant was chosen to be $\beta = 0.1$. The lattice has closed boundary conditions and the red dots determine the path of the skyrmion.

In Figure 3.7 we can see that the velocity of the skyrmion has its main component in the direction of the current and a small component in positive y-direction, known as the skyrmion Hall effect [36]. The component in y-direction depends on the chosen non-adiabatic constant β as one can see in the figures in the Appendix. For $\beta < \alpha$ the velocity has a component in $-y$-direction, for $\beta > \alpha$ in $+y$-direction and in the case of $\beta = \alpha$ we get no transverse component, in this case the third term of the implicit LLG equation (Equation 1.3) cancels out. We can also see by eye that the diameter of the skyrmion decreases when a current is applied.

A potential use case for moving skyrmions with spin-polarised currents is skyrmion based memory. skyrmion based memory is realised by nucleation and motion of skyrmions on an atom layer, called nanotrack. Therefore we will study the motion of skyrmions on nanotracks in the following.

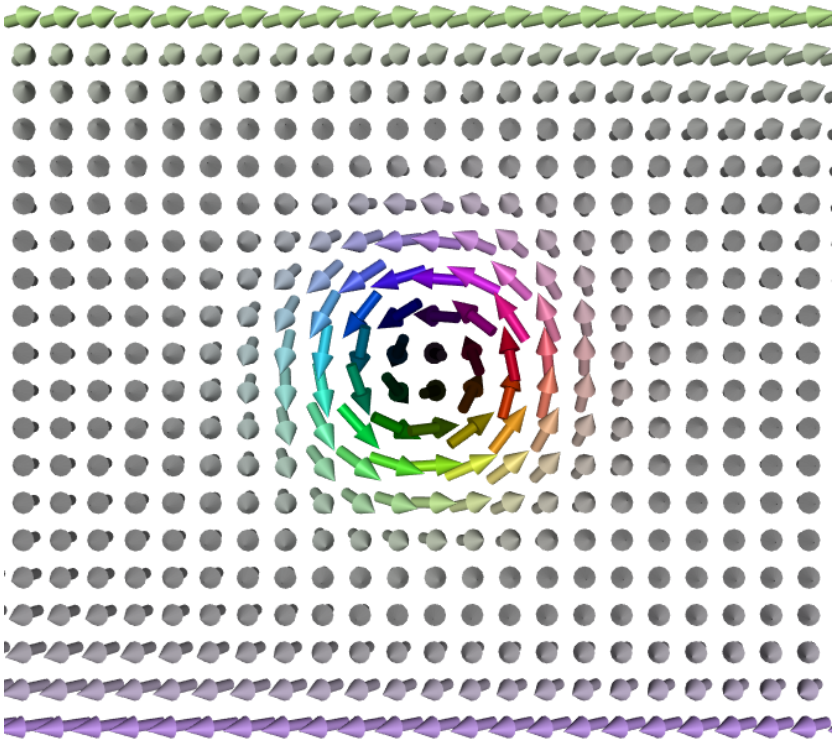

FIGURE 3.8 – Skyrmion on a nano-track

This picture shows our experimental setup, a Bloch type skyrmion on a 200×20 nano-track, the tilting of the spins at the edges is produced by the DMI. The picture was taken with *Spirit*.

For this experiment a small 200×20 lattice points nanotrack with a single skyrmion on one site was set up, see Figure 3.8, and a spin-polarised in-plane current was applied in positive x-direction (left to right). Since the track is relatively small, the skyrmion only moves a very small distance in $+y$-direction (for values of $\beta > \alpha$, respectively in $-y$-direction for $\beta < \alpha$), transverse to the spin current direction before the DMI which tilts the spins at the edges of the track acts against the transverse movement and forces the skyrmion to travel in the direction of the applied current. For large current densities u and high non-adiabatic parameters β, the skyrmion can reach the upper edge and is expelled. This also applies for the end of the track, in the case of high current densities the skyrmion can get expelled at the end of the track. Otherwise, if the skyrmion remains on the track it gets reflected at the end and bounces at the edge a few times before finding an equilibrium state, as seen in Figure 3.9.

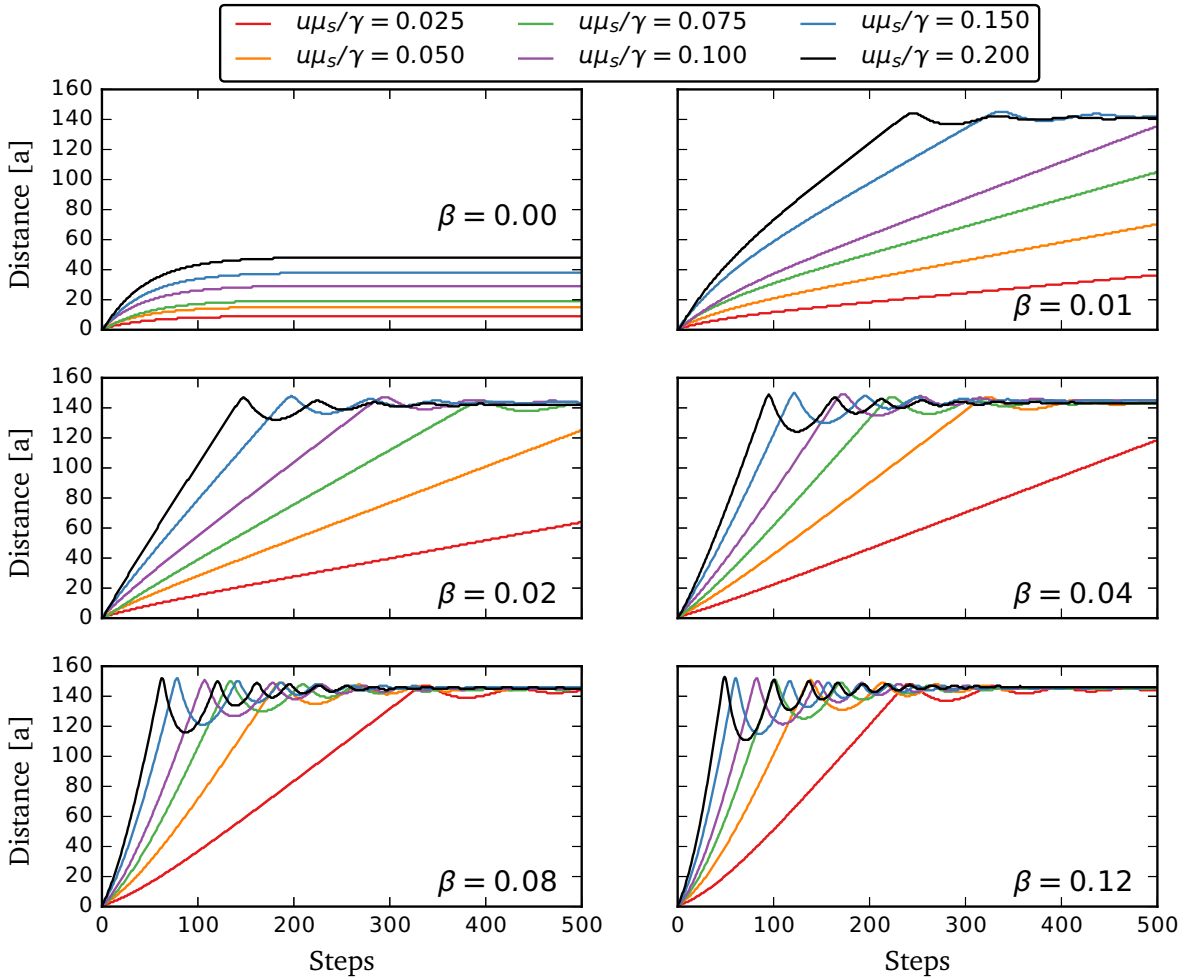

FIGURE 3.9 – Skyrmion on short nanotrack, distance over time steps

The graphs show the distance travelled by the skyrmion for different spin currents and non-adiabatic parameters. $u\mu_s/\gamma$ is proportional to the spin current magnitudes.

We simulated (Figure 3.9) spin-polarised in-plane currents for different current densities and different values of the non-adiabatic parameter β. The Gilbert damping was set to $\alpha = 0.02$. For $\beta = 0$ we observed no steady motion.

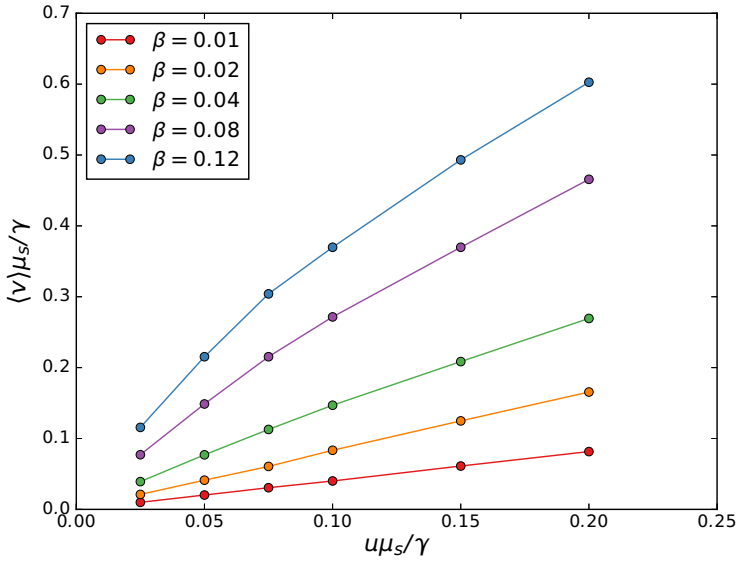

FIGURE 3.10 – Skyrmion velocity on a short nanotrack

The final steady velocity of the skyrmion for different spin current magnitudes. Open boundary conditions in x- and y-direction.

In Figure 3.10 we can see a linear dependence of the velocity for $\beta = 0.01, 0.02, 0.04$. For $\beta = 0.08$ and $\beta = 0.12$ we would expect the same dependence, but obtain smaller velocities, the derivation can be explained with the length of the nanotrack, as one can see in Figure 3.9, the skyrmion seems not to reach its maximum velocity before reaching the end of the track.

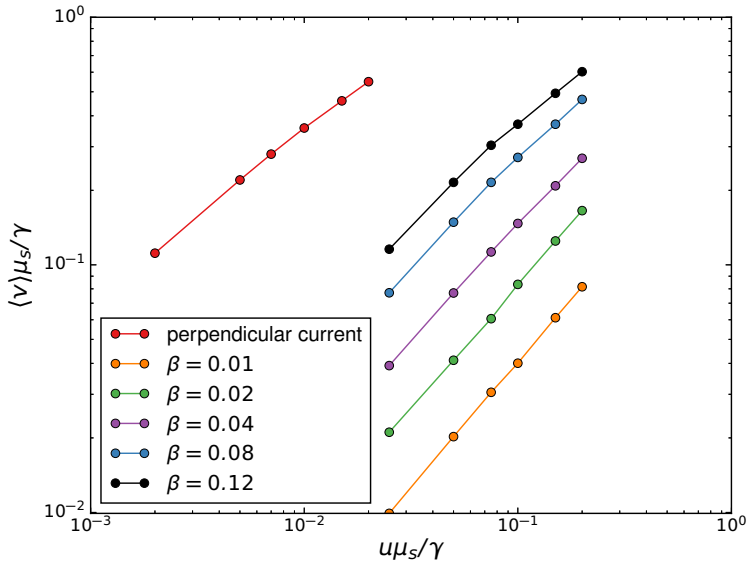

FIGURE 3.11 – Comparison of skyrmion velocity for in-plane and perpendicular current

Double log representation of the skyrmion velocity for certain spin current amplitudes. The effect of in-plane current is compared to perpendicular current simulated with the implementation of Daniel Schürhoff [18].

In Figure 3.11 the skyrmion motion with in-plane current is compared to skyrmion motion with current perpendicular to the nano-track. The current densities needed to reach a high velocity are much higher for in-plane current than for perpendicular current. To plot both currents, in-plane and perpendicular, in dependence of u we used the relation between the pre factors of the two spin current models obtained at the end of Section 2.3, considering a layer thickness equal to the lattice constant $t_x = 1$. In the case of very thick layers (t_x), one would probably obtain higher velocities for the same current applied in-plane, rather than perpendicular to the plane.

To observe the maximum velocity of the skyrmion we simulated an infinite nanotrack by applying closed boundary conditions in x-direction. The results are shown in Figure 3.12.

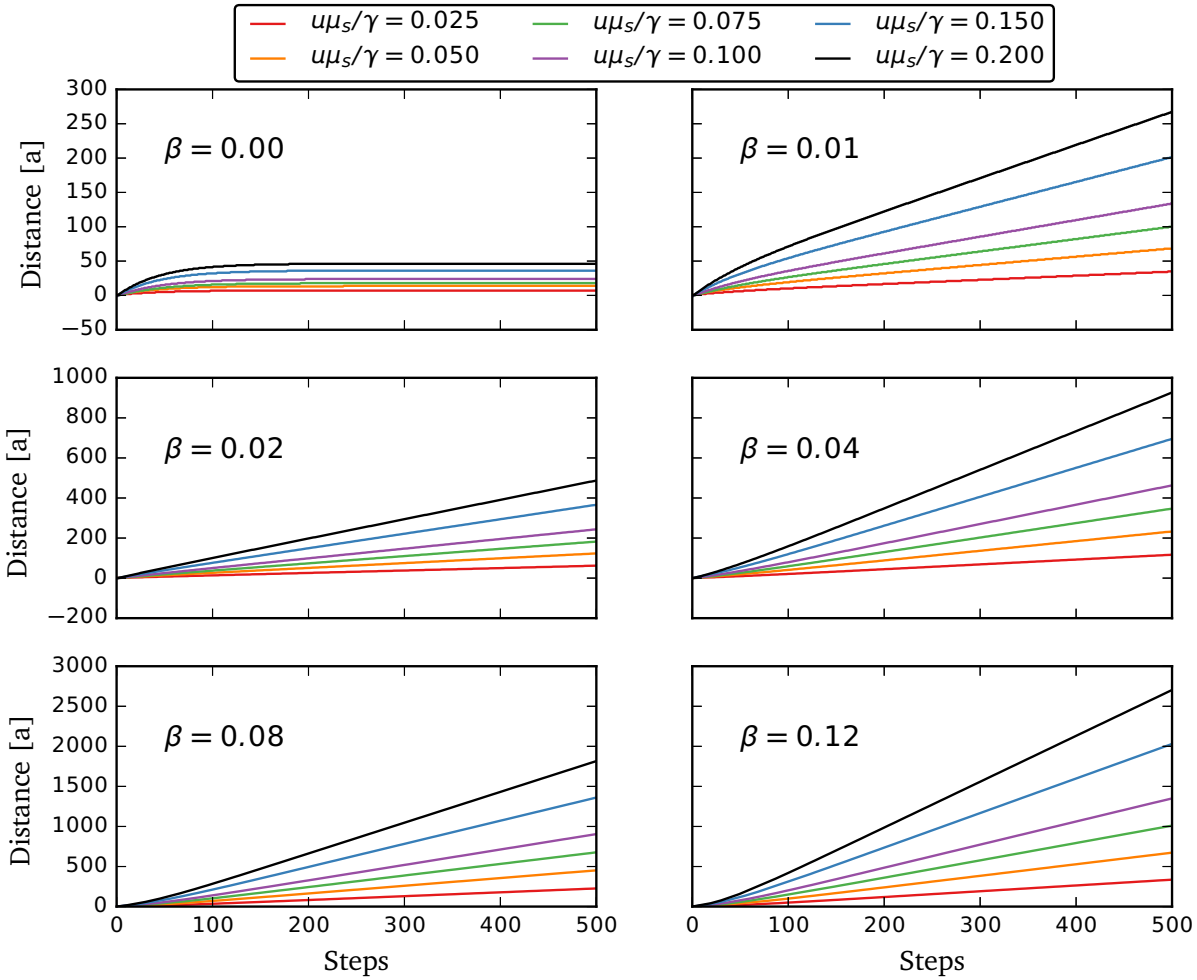

FIGURE 3.12 – Skyrmion on nanotrack, distance over time steps

The graphs, similar to Figure 3.9, show the distance travelled by the skyrmion for different spin currents and non-adiabatic parameters β on a nanotrack with closed boundary conditions in x-direction. The steps are 1/500ns, what leads to a simulated time of 1ns.

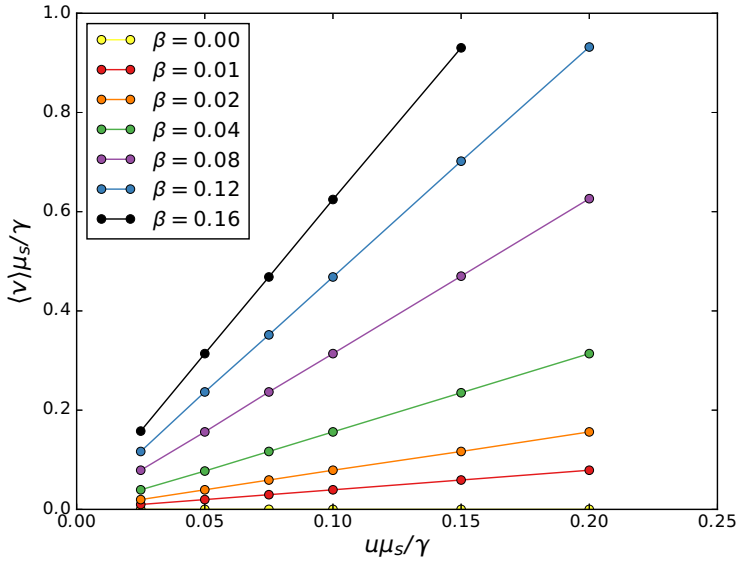

FIGURE 3.13 – Skyrmion velocity on a nanotrack

The maximum steady velocity of the skyrmion for different spin current magnitudes. The nano-track has closed boundary conditions in current-/(x-)direction and closed boundary conditions in y-direction. For $\beta = 0.16$ and a current of $u\mu_s/\gamma = 0.2$ the force towards the upper edge of the track suffices to destroy the skyrmion.

For open boundary conditions in x-direction, we now observe constant slopes for all non-adiabatic parameters β.

From the slopes in Figure 3.13, the following can be derived for the velocity of the skyrmion:

$$v = 0.78\frac{\beta}{\alpha}u\,. \tag{3.3}$$

CONCLUSION 4

In Chapter 1 the model, which this work is based on, is introduced. Ensuing in Chapter 2, first the derivation of the SIB method is detailed and the inclusion of the spin current terms is justified. The spin currents are modelled with the gradient method. The gradient method is based on a spatial gradient and the connection between the spatial gradient and the difference quotient is shown. The difference quotient is then used to give a transition from a model of STT-induced spin current perpendicular to a monolayer to the gradient method.

In Chapter 3 results from numerical experiments with the implemented method are presented. The implementation of the mentioned model for spin-polarised currents into the spin simulation framework *Spirit* has been validated by reproducing the results of Schieback *et al.* [20], before using it to simulate skyrmion movement caused by in-plane currents on nanotracks. The first experiment performed on a quadratic lattice with closed boundary conditions delivered qualitative insights about skyrmion motion induced by in-plane currents. Since skyrmion motion on nanotracks is of particular interest, especially regarding magnetic data storage devices, numerical experiments on a small nanotrack were performed and evaluated quantitatively. The behaviour of such a system for different non-adiabatic parameters was quantified with respect to the velocity of a single skyrmion and additionally the case of no steady motion ($\beta = 0$) and destruction of the skyrmion, at the edge of the nanotrack, for high velocity was observed, however nucleation was not observed. Probably higher current densities are needed. Additionally a comparison between motion induced by in-plane and perpendicular spin current was made and higher velocitys for smaller currents. skyrmion motion on an "infinite" nanotrack (closed boundary conditions in current direction) was simulated to obtain precise values for the velocity.

Henceforth other properties of skyrmion motion, for instance contact with impurities or motion of multiple skyrmions on a single track, can be investigated. The gradient method can also be used to model spin currents

in bulk material, this provides the capability to investigate the effect of spin-polarised currents on 3D spin structures and probably leads to more realistic results for a perpendicular current in thicker films. Furthermore the implementation of the spin current can be extended to describe spin currents on more complex lattices, which cover a wider range of materials.

APPENDIX

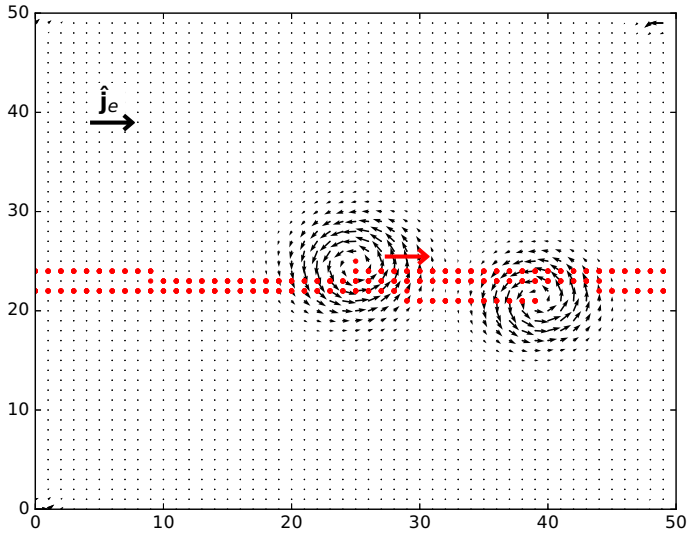

FIGURE .1 – Skyrmion motion with closed boundary conditions

Initial skyrmion position and position after 0.98ns. The applied current was $u = 0.04$ and non-adiabatic constant $\beta = 0$.

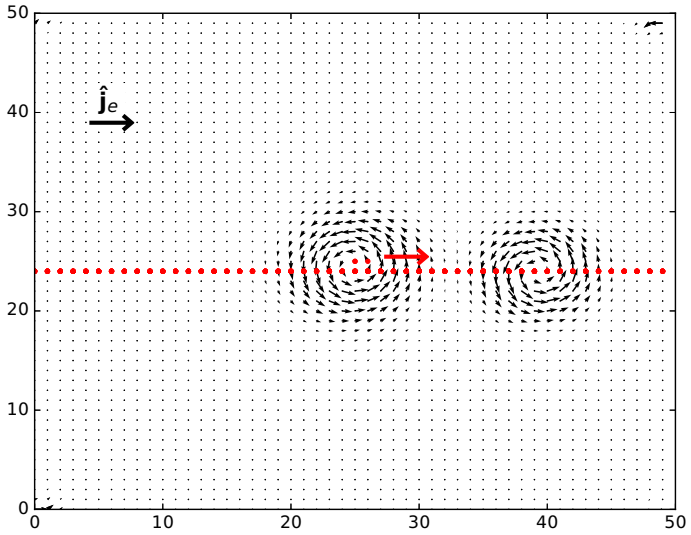

FIGURE .2 – Skyrmion motion with closed boundary conditions

Initial skyrmion position and position after 0.98ns. The applied current was $u = 0.04$ and non-adiabatic constant $\beta = 0.02$.

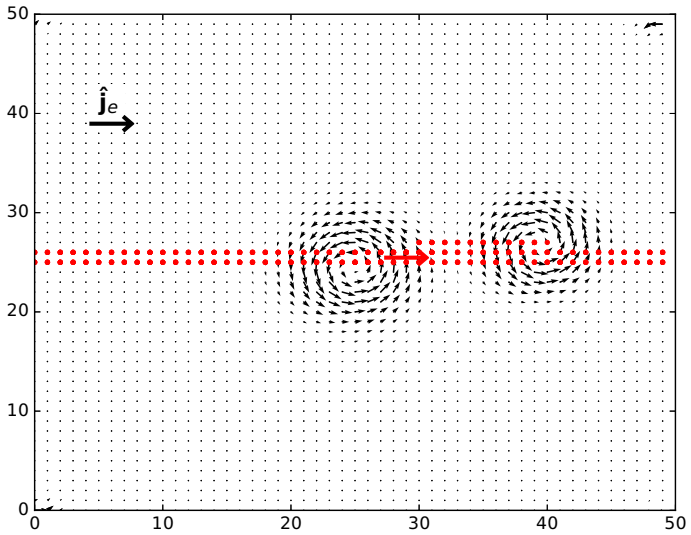

FIGURE .3 – Skyrmion motion with closed boundary conditions

Initial skyrmion position and position 0.98ns. The applied current was $u = 0.04$ and non-adiabatic constant $\beta = 0.04$.

BIBLIOGRAPHY

[1] Advanced information. *Nobelprize.org*. URL https://www.nobelprize.org/nobel_prizes/physics/laureates/2016/advanced.html.

[2] I Dzyaloshinsky. A thermodynamic theory of "weak" ferromagnetism of antiferromagnetics. *Journal of Physics and Chemistry of Solids*, 4 (4):241–255, 1958.

[3] AN Bogdanov and DA Yablonskii. Thermodynamically stable "vortices" in magnetically ordered crystals. the mixed state of magnets. *Zh. Eksp. Teor. Fiz*, 95:182, 1989.

[4] NS Kiselev, AN Bogdanov, R Schäfer, and UK Rößler. Chiral skyrmions in thin magnetic films: new objects for magnetic storage technologies? *Journal of Physics D: Applied Physics*, 44(39):392001, 2011.

[5] A Bogdanov and A Hubert. The properties of isolated magnetic vortices. *physica status solidi (b)*, 186(2):527–543, 1994.

[6] A Bogdanov and A Hubert. The stability of vortex-like structures in uniaxial ferromagnets. *Journal of Magnetism and Magnetic Materials*, 195(1):182–192, 1999.

[7] UK Rößler, AN Bogdanov, and C Pfleiderer. Spontaneous skyrmion ground states in magnetic metals. *Nature*, 442(7104):797–801, 2006.

[8] Ulrich K Rößler, Andrei A Leonov, and Alexei N Bogdanov. Chiral skyrmionic matter in non-centrosymmetric magnets. In *Journal of Physics: Conference Series*, volume 303, page 012105. IOP Publishing, 2011.

[9] FN Rybakov, AB Borisov, and AN Bogdanov. Three-dimensional skyrmion states in thin films of cubic helimagnets. *Physical Review B*, 87(9):094424, 2013.

[10] MN Wilson, AB Butenko, AN Bogdanov, and TL Monchesky. Chiral skyrmions in cubic helimagnet films: The role of uniaxial anisotropy. *Physical Review B*, 89(9):094411, 2014.

[11] XZ Yu, Y Onose, N Kanazawa, JH Park, JH Han, Y Matsui, N Nagaosa, and Y Tokura. Real-space observation of a two-dimensional skyrmion crystal. *Nature*, 465(7300):901, 2010.

[12] Spirit spin simulation framework. URL spirit-code.github.io.

[13] Stuart SP Parkin, Masamitsu Hayashi, and Luc Thomas. Magnetic domain-wall racetrack memory. *Science*, 320(5873):190–194, 2008.

[14] Stuart Parkin and See-Hun Yang. Memory on the racetrack. *Nature Nanotechnology*, 10(3):195–198, 2015.

[15] J Sampaio, V Cros, S Rohart, A Thiaville, and A Fert. Nucleation, stability and current-induced motion of isolated magnetic skyrmions in nanostructures. *Nature Nanotechnology*, 8(11):839–844, 2013.

[16] Xichao Zhang, GP Zhao, Hans Fangohr, J Ping Liu, WX Xia, J Xia, and FJ Morvan. Skyrmion-skyrmion and skyrmion-edge repulsions in skyrmion-based racetrack memory. *Scientific Reports*, 5, 2015.

[17] Theodore L Monchesky. Skyrmions: detection with unpolarized currents. *Nature Nanotechnology*, 10(12):1008, 2015.

[18] Daniel Schürhoff. Atomistic spin dynamics with real time control of simulation parameters and visualisation. 2016. URL http://www.fz-juelich.de/pgi/pgi-1/DE/Leistungen/MasterDiplomDr/_node.html.

[19] JH Mentink, MV Tretyakov, A Fasolino, MI Katsnelson, and Th Rasing. Stable and fast semi-implicit integration of the stochastic landau–lifshitz equation. *Journal of Physics: Condensed Matter*, 22 (17):176001, 2010.

[20] C. Schieback, M. Kläui, U. Nowak, U. Rüdiger, and P. Nielaba. Numerical investigation of spin-torque using the heisenberg model. *The European Physical Journal B*, 59(4):429–433, Mar 2007. ISSN 1434-6036. doi: 10.1140/epjb/e2007-00062-2. URL http://dx.doi.org/10.1140/epjb/e2007-00062-2.

[21] LALE Landau and Evgeny Lifshitz. On the theory of the dispersion of magnetic permeability in ferromagnetic bodies. *Phys. Z. Sowjetunion*, 8(153):101–114, 1935.

[22] Anonymous. Abstracts of papers to be presented at the 1955 thanksgiving meeting at the university of chicago, chicago, illinois, november 25 and 26, 1955. *Phys. Rev.*, 100:1235–1235, Nov 1955. doi: 10.1103/PhysRev.100.1235. URL https://link.aps.org/doi/10.1103/PhysRev.100.1235.

[23] T. L. Gilbert. A phenomenological theory of damping in ferromagnetic materials. *IEEE Transactions on Magnetics*, 40(6):3443–3449, Nov 2004. ISSN 0018-9464. doi: 10.1109/TMAG.2004.836740.

[24] A Thiaville, Y Nakatani, J Miltat, and N Vernier. Domain wall motion by spin-polarized current: a micromagnetic study. *Journal of Applied Physics*, 95(11):7049–7051, 2004.

[25] S Zhang and Z Li. Roles of nonequilibrium conduction electrons on the magnetization dynamics of ferromagnets. *Physical Review Letters*, 93(12):127204, 2004.

[26] A Thiaville, Y Nakatani, J Miltat, and Y Suzuki. Micromagnetic understanding of current-driven domain wall motion in patterned nanowires. *EPL (Europhysics Letters)*, 69(6):990, 2005.

[27] Z Li and S Zhang. Domain-wall dynamics driven by adiabatic spin-transfer torques. *Physical Review B*, 70(2):024417, 2004.

[28] Zhe An, FQ Liu, Y Lin, and C Liu. The universal definition of spin current. *Scientific reports*, 2:388, 2012.

[29] Gideon Müller. Exploration of skyrmion energy landscapes. 2015. URL http://www.fz-juelich.de/pgi/pgi-1/DE/Leistungen/MasterDiplomDr/_node.html.

[30] P. Chureemart, R. F. L. Evans, and R. W. Chantrell. Dynamics of domain wall driven by spin-transfer torque. *Physical Review B*, 83 (18), 2011. ISSN 1098-01211550-235X. doi: 10.1103/PhysRevB.83.184416. URL https://journals.aps.org/prb/abstract/10.1103/PhysRevB.83.184416.

[31] Z. Li and S. Zhang. Domain-wall dynamics and spin-wave excitations with spin-transfer torques. *Physical Review Letters*, 92(20), May 2004. ISSN 1079-7114. doi: 10.1103/physrevlett.92.207203. URL http://dx.doi.org/10.1103/PhysRevLett.92.207203.

[32] Shufeng Zhang, PM Levy, and A Fert. Mechanisms of spin-polarized current-driven magnetization switching. *Physical Review Letters*, 88 (23):236601, 2002.

[33] Norman L Schryer and Laurence R Walker. The motion of 180 domain walls in uniform dc magnetic fields. *Journal of Applied Physics*, 45 (12):5406–5421, 1974.

[34] Yoshinobu Nakatani, André Thiaville, and Jacques Miltat. Faster magnetic walls in rough wires. *Nature Materials*, 2(8):521, 2003.

[35] Robert Wieser, Ulrich Nowak, and Klaus-Dieter Usadel. Domain wall mobility in nanowires: Transverse versus vortex walls. *Physical Review B*, 69(6):064401, 2004.

[36] Gen Yin, Yizhou Liu, Yafis Barlas, Jiadong Zang, and Roger K Lake. Topological spin hall effect resulting from magnetic skyrmions. *Physical Review B*, 92(2):024411, 2015.

DECLARATION

I hereby declare that this thesis is my original work and it has been written by me in its entirety. I have acknowledged all the sources of information which have been used in the thesis.

Forschungzentrum Jülich, July 2017

Constantin Dißelkamp